



APPLIED SCIENCES AND ENGINEERING

Distributed sensing along fibers for smart clothing

Brett C. Hannigan*, Tyler J. Cuthbert, Chakaveh Ahmadizadeh, Carlo Menon*

Textile sensors transform our everyday clothing into a means to track movement and biosignals in a completely unobtrusive way. One major hindrance to the adoption of “smart” clothing is the difficulty encountered with connections and space when scaling up the number of sensors. There is a lack of research addressing a key limitation in wearable electronics: Connections between rigid and textile elements are often unreliable, and they require interfacing sensors in a way incompatible with textile mass production methods. We introduce a prototype garment, compact readout circuit, and algorithm to measure localized strain along multiple regions of a fiber. We use a helical auxetic yarn sensor with tunable sensitivity along its length to selectively respond to strain signals. We demonstrate distributed sensing in clothing, monitoring arm joint angles from a single continuous fiber. Compared to optical motion capture, we achieve around five degrees error in reconstructing shoulder, elbow, and wrist joint angles.

INTRODUCTION

Soft strain sensors have become an active research area in part because their use in “smart textiles” is needed to achieve movement tracking in next-generation wearable devices. Topical applications of wearable strain sensors include kinematics monitoring, pose estimation, and the measurement of mechanically transduced biosignals (e.g., heart rate and speech) (1–4). Soft sensor arrays have been used to map pressure and to provide feedback for soft robotics and in human interface devices (5, 6). Sensing movement through textiles is unique and has potential for high impact in advancing our ability to track athletics and monitor health (7). Clothing—in comparison to other wearable technology that is attached directly to the body or uses rigid components such as exoskeletons—has inherent variability including folds, nonhomogeneity in body contact (e.g., tightness and looseness), and confounding mechanical strain (e.g., pressure, stretch, and twisting). To combat this limitation of clothing, there has been a focus on increasing the number of sensing elements around the location of focus to increase monitoring accuracy. For example, the current state of the art in upper-body joint angle tracking with wearable sensors requires three to eight sensors per joint for angle estimation (8, 9). To have high spatial resolution without an impractically high number of connections, sensor arrays are often used. Ever-denser arrays are pursued for finer resolution in soft pressure sensors (10). However, as the number of sensing locations is increased, complexity increases because many sensors and connections are required. The factors limiting the scaling up of the density of sensors are often the amount of space available on the garment for sensors and interconnections and the method for reliably connecting these sensors and accessing their signals. Connections between textiles and rigid electronics are particularly troublesome because the high stress at the interface makes them prone to failure (11, 12). Arrays introduce other problems such as cross-talk between channels, which can limit their resolution (13).

What makes textile sensors most attractive is their ability to transform the clothing we wear every day into functionalized devices with absolutely minimal obtrusiveness. Full textile integration is necessary to achieve widespread adoption of ubiquitous “smart”

garments in sports, rehabilitation, occupational health, and everyday life. This integration requires the reduction and eventual elimination of rigid electronic components on the garment and constrains the design to what would be attainable with entrenched industrial textile production methods. The sustainability of functional textiles is subject to increased recent scrutiny because of the large amount of waste associated with their eventual disposal coupled with the various advanced materials e-textiles may contain (14). Separation of these materials for recycling is difficult, so there exist two main ways to address this challenge: making separation at end-of-life easier or moving toward using a single material (15). The distributed sensing approach has promise to address some of these problems by replacing discrete interconnects and electronics in the garment with single-fiber sensors. In this case, the sensing fibers themselves should ideally consist of the same materials as the bulk garment, preferentially using biodegradable or easily separable polymers, and be made with cleaner fabrication processes. Continuous fibers able to sense at multiple points along their length that can be woven or knit into fabric would greatly reduce connection issues, allow greater sensor density, potentially increase sustainability, and maintain compatibility with established textile processes. It follows that achieving these goals would thereby increase the reliability and lower the cost of smart textile garments.

Distributed strain sensing

Distributed sensing is a promising solution to these aforementioned problems encountered when scaling up strain and pressure sensing garments. A distributed sensing system permits multiple measurements out of a single sensor element, each localized in space. Unlike approaches using multiple sensors connected by wires, multiplexers, or switches, the electrical connectivity is greatly simplified (16, 17). Distributed sensing can also be used to increase sensitivity (18, 19), allow arbitrarily high spatial resolution (20), and simplify two-dimensional (2D) pressure or strain sensitive arrays (16, 20, 21). Capacitive strain sensors have garnered recent interest because the configuration is possible in yarn, coaxial, or twisted fiber form and has linear response to strain, which is ideal for integration into textiles (22–25). Distributed strain sensing has been shown with promising bench tests using chains of soft capacitive strain sensors (17). Segmented soft capacitive sensors can be used to isolate strain at individual segments through microfracturing of piezoresistive electrodes

Biomedical and Mobile Health Technology Laboratory, Department of Health Sciences and Technology, ETH Zurich, Lengghalde 5, 8008 Zurich, Switzerland.

*Corresponding author. Email: brett.hannigan@hest.ethz.ch (B.C.H.); carlo.menon@hest.ethz.ch (C.H.)

Copyright © 2024 the Authors, some rights reserved; exclusive licensee American Association for the Advancement of Science. No claim to original U.S. Government Works. Distributed under a Creative Commons Attribution NonCommercial License 4.0 (CC BY-NC).

(19). Distributed pressure sensitive arrays have been demonstrated using frequency domain measurements of resistor-inductor-capacitor (RLC) resonator chains with a breadth of sensing applications (26). The RLC approach has yet to address the elimination of rigid electronic components on the sensing element, and it requires a parallel connectivity of multiple resonant circuits, meaning that it would be difficult to both implement using fully soft electronics and transform into a linear fiber. Another method we may classify as “pseudo-distributed” sensing uses algorithms to extrapolate localized strain from the DC resistance of a piezoresistive sensor (27). This technique shows impressive results for classifying sets of repeatable patterns using a piezoresistive nanomesh sensor (28), but it is fundamentally not possible to reconstruct arbitrary, independent localized strains from single-port DC resistance measurements. However, piezoresistive strain sensors (e.g., using graphene nanofilms) (29, 30) may also be used for distributed sensing with frequency-domain impedance measurements. Applying techniques from electrical impedance tomography, a sensor mesh made from kinesiology tape coated with graphene nanofilms can be interrogated to obtain a continuous 2D strain map (31). This greatly increases the information collected from the sensing mesh but requires a series of perimeter connections. Here, we aim instead to eliminate the majority of unreliable connection points and increase textile integration with a 1D fiber. Distributed sensing is yet to be integrated as a fiber into a textile garment or as a wearable system. We desired to build upon these results and apply distributed strain sensing methods along a fiber that is highly suitable for textile integration.

Here, we demonstrate a system to enable distributed sensing along a strain sensor and a prototype garment that monitors the three major arm joint angles with one continuous sensing fiber. Our solution isolates the single pair of connections to one end of the stretchable fiber, so that the fiber may be sewn or woven into a textile without connections or wires in the fabric. This fiber sensor design allows the single remaining connection to be centralized at one end in a proximal hub location. It compares favorably to some other fiber strain sensor designs that require wires from both ends or access to an inner layer (e.g., coaxial capacitive fibers), which brings much greater complexity to textile manufacturing. We can envision extending the prototype to include many functionalized fibers in the garment, for example, to greatly increase sensor density or instrument multiple extremities, as illustrated conceptually in Fig. 1. We further developed a compact electronic impedance analyzer circuit to collect high-speed impedance measurements at multiple frequencies in parallel and use this device to develop an algorithm and test fixture to quantify strain reconstruction performance more rigorously. We show the application of a single-fiber capacitive sensor with tunable sensitivity at different locations along its length, which further increases the capabilities of our distributed sensing system. We combine these into a prototype garment that can monitor the angles of the shoulder, elbow, and wrist joints with high accuracy on a single channel.

RESULTS

A sensing fiber with selective response to strain

While in the general case, distributed sensing methods may be applied to various transduced phenomena of interest—potentially with a multidimensional sensor configuration—here, we limit our focus to strain sensing distributed in 1D along the axis of a fiber, as

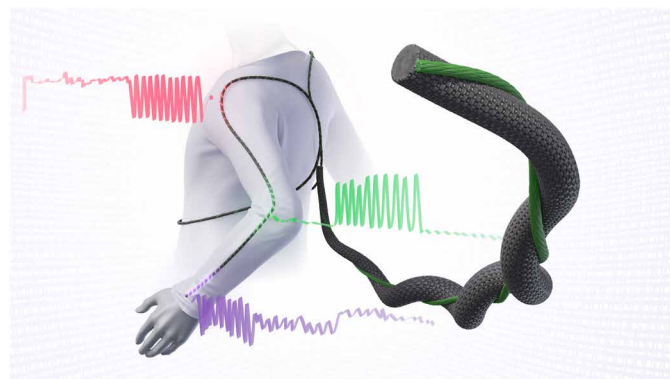


Fig. 1. A conceptual illustration of our distributed sensing approach used to measure the three major joint angles of the arm, with an envisioned extension of the sensing fiber around the torso.

these are the atomic components of textiles. A distributed strain sensing fiber designed to be incorporated into textiles should be highly sensitive and compatible with existing textile processing methods. While the fiber itself may follow a long path along the garment, the desired strain information to isolate a movement of interest is often concentrated in few areas along the fiber's length (e.g., around the joints). Thus, we desired our sensing fiber to have spatial specificity to strain at certain locations. We previously reported a previously unexplored capacitive fiber strain sensing modality (32) having some attractive features that can be used for distributed sensing applications. These are (i) leveraging the auxetic behavior of a helical yarn complex to achieve a higher sensitivity than expected for typical capacitive strain sensors; (ii) the ability to tune this sensitivity by manipulating the helical pitch; and (iii) high robustness to stress and suitability for a reel-to-reel manufacturing process. These helical auxetic capacitive sensor (HACS) fibers are composed of an inextensible conductor coiled around a conductive elastomer core. The core is an ordinary polyester wrapped elastane fiber, coated with polypyrrole using a low-waste vapor phase process. Copper wire is used as the inextensible conductor coil, as it has the ideal mechanical properties and an insulating enamel layer to achieve the desired capacitor configuration. The highly robust copper wire wrapping also limits the maximum strain of the sensor fiber, so that the polymer core does not plastically deform. Exchanging the copper wire component for a conductive yarn/thread is possible, although not within the scope of this research. Upon straining, the elastomer core stretches, while the inextensible wrapping increases in pitch and decreases in helical diameter. At higher strains, the inextensible component becomes nearly straight, causing the coils to “flip” so that the elastomer is coiled around it. The “flipping” increases the overall outer diameter with increasing strain; this is an example of auxetic material behavior. These mechanics are shown in Fig. 2B and can allow one to access a larger gauge factor (GF) than ordinarily seen for capacitive strain sensors, which are typically limited by geometry to unity GF (33). The GF is defined in Eq. 1, where $C(\epsilon)$ is the capacitance at strain $\epsilon = \ell/\ell_0$ and $C(0)$ is the unstrained capacitance. Full details about the sensor fiber fabrication may be found in Materials and Methods. More important for this work than sheer sensitivity is the ability to manipulate the GF along the sensor by adjusting the helical pitch. Our previous HACS was each only of a single pitch and therefore a single sensitivity. In this research, we modified the

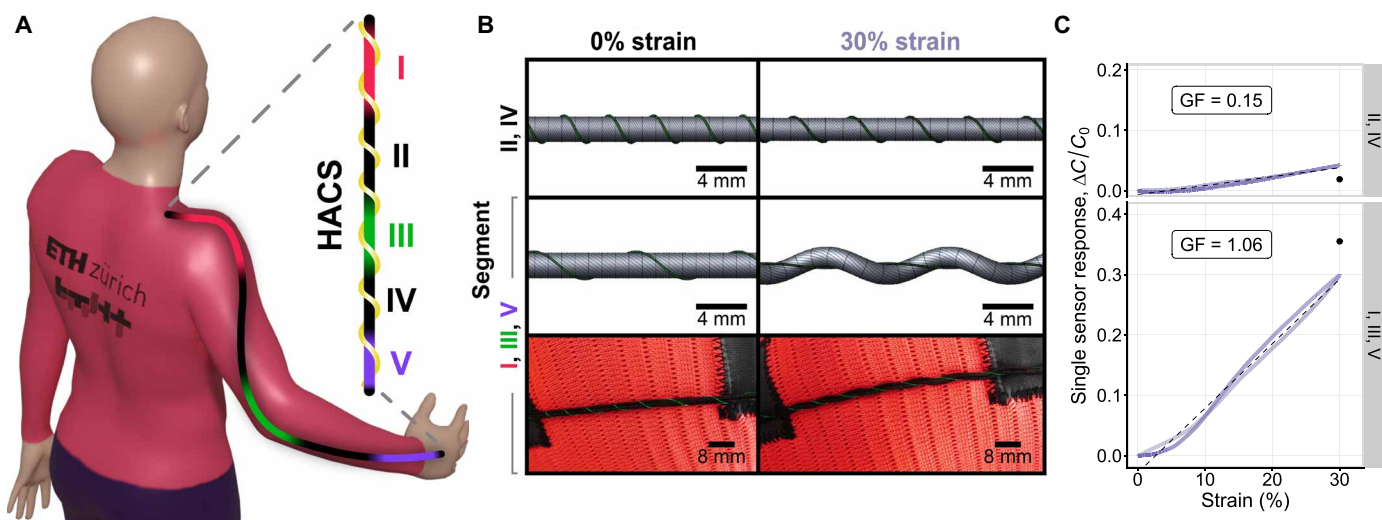


Fig. 2. Prototype garment and sensing fiber. (A) Rendering of the path of the sensor along the arm, where I, III, and V indicate the high-sensitivity regions around the shoulder, elbow, and wrist joints, respectively. (B) Top: Geometric modeling of the HACS sensor low-sensitivity (II and IV: 3.5-mm pitch) and high-sensitivity (I, III, and V: 8-mm pitch) regions under relaxed and 30% strain conditions; Bottom: Photographs of the unstrained and strained sensor in the garment at the elbow joint. (C) Response versus strain plots (solid), GF (dashed black), and computational model predictions (round black marker) for the respective HACS sensitivity regions [model adapted from our previous work (32)].

HACS such that we changed the pitch throughout a single fiber to achieve different sensitivities in different locations. This is a novel approach to fabricating HACS and using our previous research.

$$GF = \frac{[C(\epsilon) - C(0)] / C(0)}{\epsilon} \quad (1)$$

We devised a prototype garment by instrumenting a long-sleeved athletic shirt with a HACS fiber running from the shoulder to wrist (approximate path shown in Fig. 2A). We desire to monitor the three major angles of the arm as a proof of concept: shoulder adduction, elbow flexion, and wrist flexion. As described in (32), the GF of these fiber sensors may be tuned by adjusting the helical pitch. We decided to use this to our advantage by manipulating the pitch in space along a single continuous fiber and more selectively respond to strains only at the joints. We chose longer, 8-mm pitch enabling high sensitivity for the regions of interest—three eight segments around the shoulder, elbow, and wrist joints (labeled as I, III, and V in Fig. 2). Because the maximum length of the sensing fiber is governed by the straightened length of the inextensible wrapping, which decreases with longer pitch values, there is a trade-off between attainable sensitivity and maximum strain. We chose the 8-mm pitch value to maximize the GF while still allowing a sufficient strain range that covers what is expected in textiles. For the rest of the sensor, a shorter 3.5-mm pitch ensures maximum insensitivity to strain at undesired locations (labeled as II and IV in Fig. 2). This type of sensor fiber has been shown to be relatively insensitive to torsion, with less than 20% change in capacitance during a full 360° of torsion (32)—torsion near this amount would not be possible when affixed to the garment. We investigated the effect of simultaneous strain and bending across different physiologically plausible bend radii to evaluate the fiber sensor's response to bending/stretching like that seen across the joints. The results show a very slight increase in signal for small bend radii, but the variability between samples is generally higher than that attributable to bending (see

section S4 and fig. S7). We further performed controlled tests to examine any degradation of sensitivity attributable to wear during cyclic durability tests. We observed very stable response and GF before and after 1000 cycles of straining to 20% (see section S5 and fig. S8). The geometry of these sensor regions when relaxed and subjected to strain is rendered using the geometrical model from (32) and is compared in Fig. 2B. The model predicts GFs of 1.18 and 0.06 for the highly sensitive and insensitive regions, respectively. Universal testing machine (UTM) tests closely agreed with respective GFs of 1.06 and 0.15, shown in Fig. 2C. Next, we briefly describe the principle by which we may discriminate localized strain along these sensing fibers using impedance measurements.

Distributed capacitive strain sensing

To use the HACS fiber in a distributed sensing application, we need to identify the mechanism by which strain at various segments along the fiber may be differentiated. As mentioned previously, distributed sensing along a resistance-capacitance (RC) transmission line model has been demonstrated on the bench (34). In the following section, we will characterize short, single sensors to determine their response to strain. Using these results, we model the predicted behavior of a chain of these sensors, using it to choose an excitation frequency band that well differentiates the localization of strain to each segment. We verify the model with measurements from the UTM and an inductance-capacitance-resistance (LCR) meter. Lastly, we validate our readout electronics against this reference.

Similar to many sensors that use capacitance to transduce strain, our fiber sensors can be considered as an electrical transmission line. The capacitance and resistance along a length of fiber are distributed in infinitesimally small segments. By approximating these with a finite number of lumped elements, we can probe a sensor with varying frequencies and use the response to estimate capacitance—and thus localized strain—at certain regions along its length. A schematic of an HACS discretized into $n = 4$ segments and the corresponding

transmission RC line model circuit are shown in Fig. 3 (A and B, respectively). An expression for the input impedance Z_i at stage $i \in \{1, \dots, n\}$ of an RC transmission line with this structure may be generated recursively as follows

$$Z_i(\omega) = \begin{cases} \frac{1}{j\omega C_i + \frac{1}{Z_{i+1}(\omega)}} + R_i & 1 \leq i < n \\ \frac{1}{j\omega C_n} + R_n & i = n \end{cases} \quad (2)$$

Each transmission line segment (or discretized stage) acts as a low-pass RC filter. Lower frequency excitation signals have less attenuation through the line, allowing the impedance of the entire line to be measured. Conversely, higher-frequency excitation signals are attenuated to a greater degree and predominantly measure the impedance of the sensing area nearer to the readout circuit. Therefore, by comparing the impedance measured at a higher frequency with a lower one, the spatial distribution of capacitance through the line may be inferred. When multiple regions are strained simultaneously, it is plausible that the capacitance change at one region may mask another, resulting in a strain reconstruction that is not unique. Other works have shown bench experiments with successful measurements from all combinations of simultaneously strained regions (17, 35). We add confidence to these findings from a theoretical perspective by analyzing the structural identifiability of the lumped model

from Fig. 3B. Structural identifiability is a general mathematical technique to determine whether it is possible to uniquely reconstruct the parameters of a system given its input signal and output measurements and is commonly applied to biological compartmental models (36) and in structural dynamics (37). Our analysis (fully detailed in section S3) indicates that the R_i and C_i parameters of the lumped sensor systems are uniquely measurable using a time-varying input signal. This theoretical method is subject to certain conditions, such as an assumption of perfect noise-free measurements, constant RC parameters, and the use of the lumped model circuit rather than the true distributed parameter system. In reality, there is always noise present, and the parameters, although slowly varying compared to the excitation, are not constant. Therefore, the unique identification of the real system's parameters may not be guaranteed. However, our mathematical analysis supports the empirical evidence in this paper and others (17) that the localized strain is uniquely reconstructable. Stretchable conductive materials such as the conductive polymer coating used here generally have substantially higher resistance compared to typical rigid/metal conductors. We may use the relatively higher resistance to more easily access strain measurements localized in space along the stretchable fiber length because the larger resistance shifts the frequency response to lower bands. Sensor characterization tests show that the piezoresistance, or increase in resistance versus strain, of the HACS fiber remains low (fig. S6C). This is important to ensure that strained

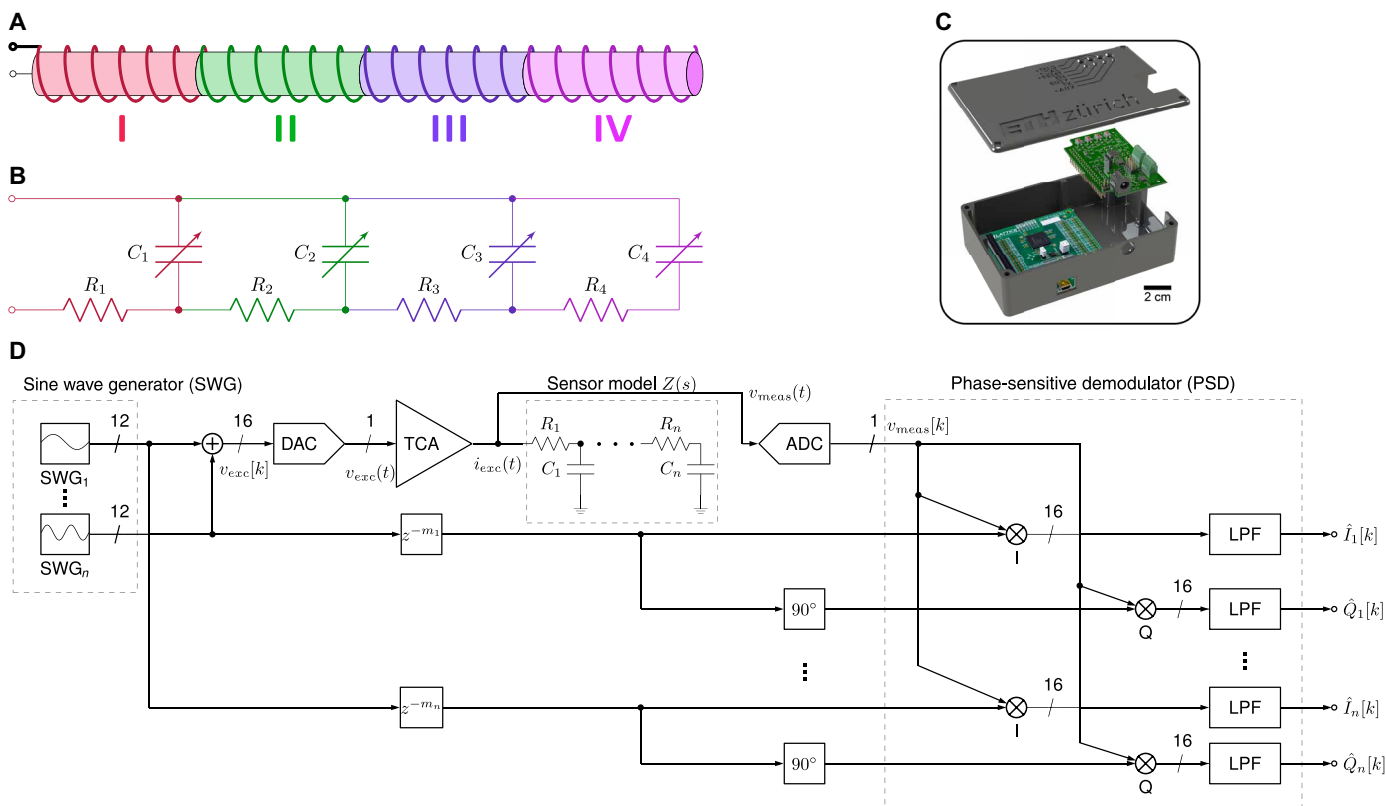


Fig. 3. Discretized sensor schematic and electronics overview and function. (A) Schematic of sensor connectivity, split into four sensing regions. (B) The corresponding RC ladder model circuit. (C) Exploded view of the readout electronics, including enclosure, analog front-end printed circuit board (PCB), and field-programmable gate array (FPGA) board. (D) Block diagram overview of the entire signal processing pathway with n frequency channels, including sine wave generator (SWG), digital-to-analog converter (DAC), sensor model circuit, analog-to-digital converter (ADC), phase-sensitive demodulator (PSD), and filtering blocks.

segments maintain sufficient conductance so that the subsequent segments further down the fiber may still be measured. We must first choose excitation frequencies—or, equivalently, manipulate the sensor’s specific resistance and capacitance—to maximize the discrimination between strains across each sensing region. We began an initial test by fabricating four 10-cm long HACSSs with pitch of approximately 4 mm; this should yield $GF \approx 0.5$ according to the model and results from our previous study (32). We measured the sensor response $\frac{\Delta C}{C(0)}$ versus strain for each sensor independently and fit a linear model to obtain relaxed capacitance $C(0)$, relaxed resistance $R(0)$, and GF for each (Fig. 4A). We then modeled the impedance of the cascaded transmission line connection of the sensors from Fig. 3A at arbitrary strain using the Cauer RC ladder transfer function (38) from Eq. 2. We allowed the resistance and capacitance parameters to vary with strain, assuming a linear relationship obtained from the single sensor tests, for example

$$C(\epsilon) = C(0)(1 + \epsilon \cdot GF)$$

The frequency response of the model at strains of 10 to 40% is shown in Fig. 4B, presented as the change in RC-parallel capacitance compared to that at $\epsilon = 0$. We observed that the frequency window of 10 kHz to 100 kHz differentiates sensor segments I to IV well with respect to strain. At frequencies below this window, the observed ΔC versus strain is large, but nearly identical behavior is seen at each segment I to segment IV. Above this window, the ΔC versus strain is uniformly low for all sensor segments. We then connected the individual segments in cascaded fashion (following the schematic of Fig. 3B) and placed them in a fixture to confirm our

model predictions. The fixture allows each sensing region to be strained independently. For the purposes of illustrating the mechanism and for device validation, we strain only one region at a time. In the “Localized strain reconstruction” section, we will also examine the case where two regions are strained simultaneously. The individual sensor segments were connected with low-resistance copper wire for during testing so that the exact same samples tested individually could also be tested in series. This is electrically equivalent to a continuous strain sensing fiber, which we used in the prototype garment that follows. An LCR meter was used to perform frequency sweeps of the system to obtain the data shown in Fig. 4C, which agree well with our simple model. As expected, as we continue down the ladder network from the readout circuit (from segments I to IV), the change in capacitance response attributable to strain at higher frequencies becomes lower. Last, we performed a similar measurement using our readout system instead of the LCR. Our device (Fig. 3C) functions as a compact, configurable impedance analyzer that measures at multiple frequencies in parallel at high speeds (around 30-Hz output data rate), compared to the LCR that measures across many frequencies with low resolution in time (seconds per sweep). We chose four excitation frequencies (approximately 12.5, 25, 50, and 100 kHz) from the frequency window we previously identified where the change in capacitance versus strain between each sensor segment is approximately maximal (see Fig. 4B). We observe a similar trend using our device as the LCR sweeps (Fig. 4D). We have now established a basis for how distributed sensing may be accomplished using impedance measurements at multiple frequencies. Next, we continue by briefly describing the signal processing background about how the system measures the

Downloaded from https://www.science.org on March 22, 2024

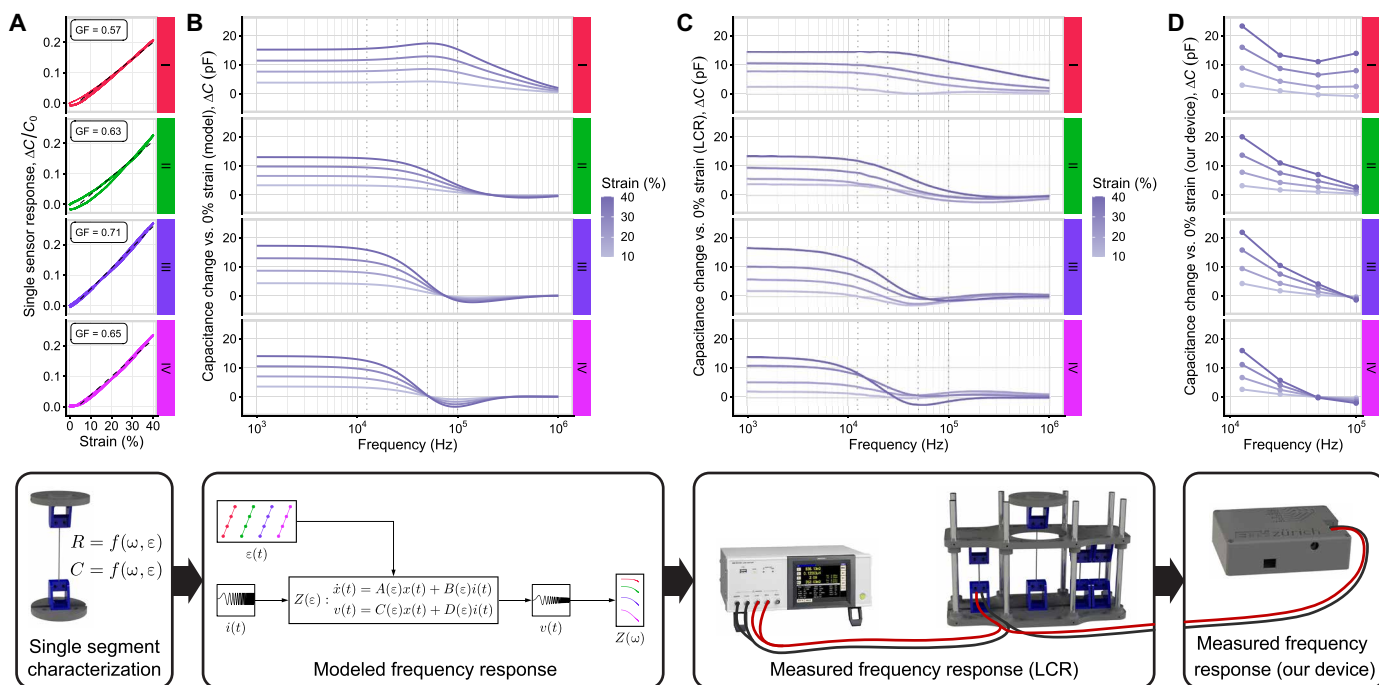


Fig. 4. Frequency separation of strain across the transmission line. (A) Response $\Delta C/C(0)$ versus strain for each sensing region, tested individually to determine the GF via a linear fit. (B) The simulated capacitance frequency response $C(\epsilon) - C(0)$ of the model circuit from Fig. 3B, using initial values and GFs from (A) under strains of 10 to 40%. (C) Corresponding frequency sweeps obtained with the LCR meter on the strain sensitive fiber samples. (D) The response evaluated using our readout system at four discrete frequencies.

impedance at multiple frequencies in parallel and with high readout speeds.

High-speed impedance measurement

Here, we describe the impedance measurement procedure used in our readout electronics. The signal processing pathway is outlined in Fig. 3D and described below. Figure 5 shows a more simplified system schematic with example signals from both simulation and measurements. A detailed description of each component's

implementation in firmware or hardware may be found in section S1. In addition, the system calibration process is outlined in section S2.

The circuit first includes a sine wave generator (SWG) that produces digital sine and cosine signals at each f_i of N_f frequencies. Using k as a discrete-time index variable and f_s for the sampling frequency, the SWG produces the signals shown in Eq. 3 (we use square bracket notation to indicate discrete-time signals and parentheses to indicate continuous time).

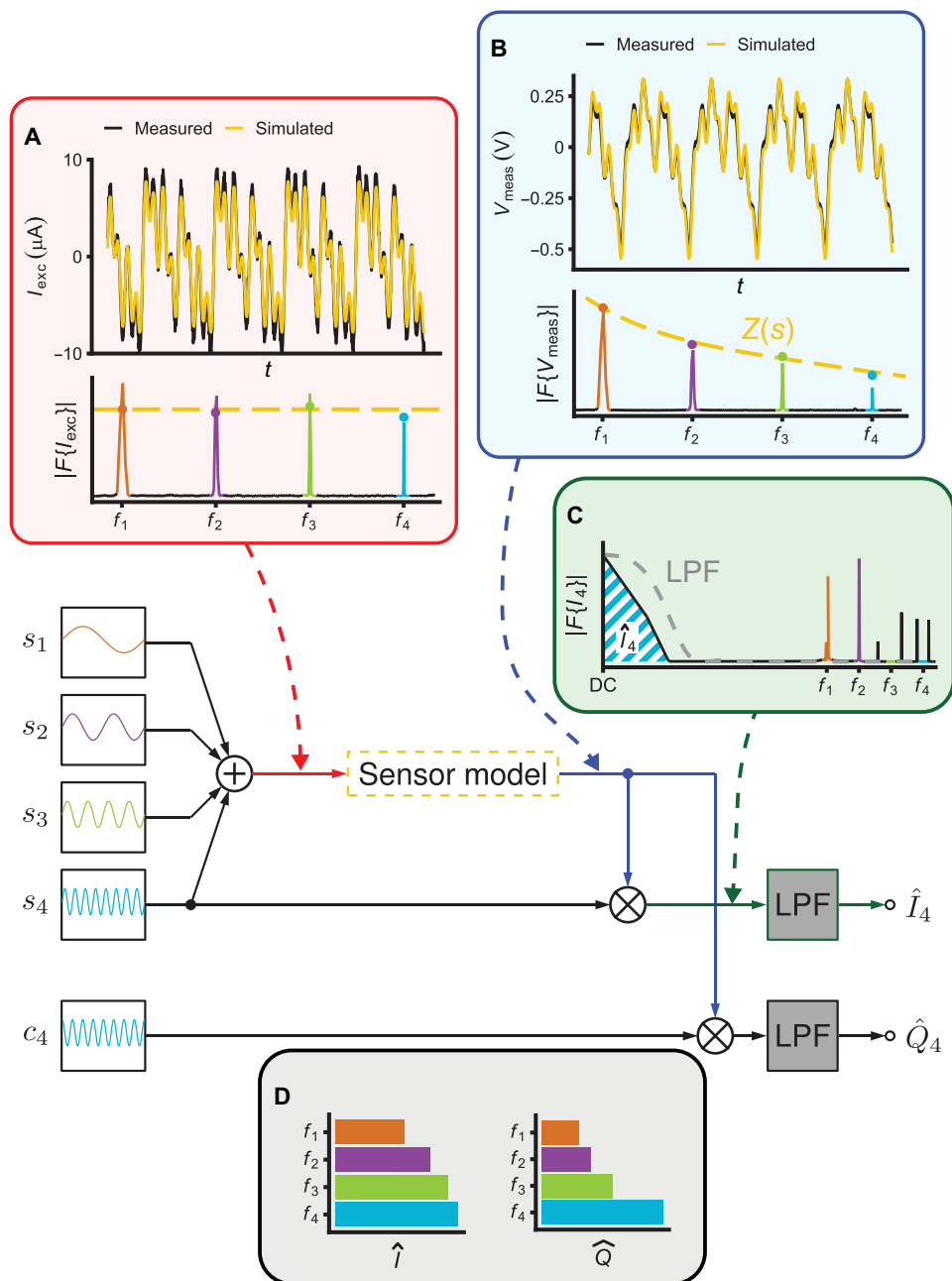


Fig. 5. Abbreviated schematic with example signals. (A) Top: Multisinusoid excitation current $i_{exc}(t)$ waveform (simulated and measured) and its Fourier transform. (B) Voltage response from the sensor $v_{meas}(t)$ (measured and simulated using the ladder model from Eq. 2) and its Fourier transform, with sensor model frequency magnitude response overlaid in dashed yellow. (C) Fourier transform of the PSD mixer output $I_4[k]$, with DC component $\hat{I}_4[k]$ shown as hatched area and approximate low-pass filter response shown in dashed gray. (D) The relative in-phase $\hat{I}[k]$ and quadrature $\hat{Q}[k]$ impedance components from the sensor model simulation.

$$\begin{aligned} s_i[k] &= \sin\left(2\pi\frac{f_i}{f_s}k\right) \quad i \in \{1, \dots, N_f\} \\ c_i[k] &= \cos\left(2\pi\frac{f_i}{f_s}k\right) \quad i \in \{1, \dots, N_f\} \end{aligned} \quad (3)$$

The digital-to-analog converter (DAC) converts the sum of the sine waves to an analog excitation voltage signal $v_{\text{exc}}(t)$. This signal satisfies the conditions of our structural identifiability analysis to uniquely determine the lumped system's RC parameters. The signal is conditioned and converted to a current signal $i_{\text{exc}}(t)$ by the transconductance amplifier (TCA), following Eq. 4. An example of this current signal is shown in Fig. 5A along with its spectrum, consisting of $N_f = 4$ frequency components of approximately equal magnitude. For simplicity, we assume a delay-less analog-to-digital converter (ADC) transfer function equal to unity and approximate the TCA transfer function as a frequency-independent gain G . The dynamics introduced by the ADC and TCA are discussed in sections S1.1 to S1.3.

$$i_{\text{exc}}(t) = G \sum_{i=1}^{N_f} s_i(t) = G \sum_{i=1}^{N_f} \sin(2\pi f_i t) \quad (4)$$

The linear, time-invariant impedance response of the sensor $Z(\jmath)$ from Eq. 2 imparts a frequency-dependent gain and phase shift for each component of the $i_{\text{exc}}(t)$ excitation signal as shown in Eq. 5, where $|Z_i|$ is the gain and φ_i is the phase shift at frequency f_i .

$$\begin{aligned} v_{\text{meas}}(t) &= \mathcal{L}^{-1}\left[Z(\jmath)I_{\text{exc}}(\jmath)\right] \\ &= G \sum_{i=1}^{N_f} |Z_i| \sin(2\pi f_i t + \varphi_i) \end{aligned} \quad (5)$$

In Fig. 5B, the resulting voltage across the sensor $v_{\text{meas}}(t)$ is shown. The magnitudes of the four frequency components are modified following the linear response of the sensor. This signal is digitized and processed by a phase-sensitive demodulator (PSD) that uses the pure sine and cosine waves from Eq. 3 as a reference to extract in-phase and quadrature components at each frequency. Using Euler's formula, the signals from Eq. 3 may be written as

$$s_i[k] = \frac{e^{j2\pi\frac{f_i}{f_s}k} - e^{-j2\pi\frac{f_i}{f_s}k}}{2j} \quad (6)$$

$$c_i[k] = \frac{e^{j2\pi\frac{f_i}{f_s}k} + e^{-j2\pi\frac{f_i}{f_s}k}}{2} \quad (7)$$

and each frequency term of Eq. 5 may be written as shown in Eq. 8.

$$v_{\text{meas}}[k] = G \sum_{i=1}^{N_f} |Z_i| \frac{e^{j2\pi\frac{f_i}{f_s}k + \varphi} - e^{-j2\pi\frac{f_i}{f_s}k - \varphi}}{2j} \quad (8)$$

The PSD mixer multiplies each term i of Eq. 6 with Eq. 8 to calculate the in-phase component. After simplification, we obtain Eq. 9.

$$\begin{aligned} I_i[k] &= s_i[k] \cdot v_{\text{meas}}[k] \\ &= \frac{G|Z_i|}{2} \left(-\frac{e^{j2\pi\frac{2f_i}{f_s}k + \varphi_i} + e^{-j2\pi\frac{2f_i}{f_s}k + \varphi_i}}{2} + \frac{e^{\varphi_i} + e^{-\varphi_i}}{2} \right) \\ &= -\frac{G|Z_i|}{2} \cos\left(2\pi\frac{2f_i}{f_s}k + \varphi_i\right) + \underbrace{\frac{G \cdot |Z_i|}{2} \cos(\varphi_i)}_{\hat{I}_i[k]} \end{aligned} \quad (9)$$

Similarly, the PSD mixer multiplies each term i of Eq. 7 with Eq. 8 to yield the quadrature component, Eq. 10.

$$\begin{aligned} Q_i[k] &= c_i[k] \cdot v_{\text{meas}}[k] \\ &= \frac{G|Z_i|}{2} \left(\frac{e^{j2\pi\frac{2f_i}{f_s}k + \varphi_i} - e^{-j2\pi\frac{2f_i}{f_s}k - \varphi_i}}{2j} + \frac{e^{\varphi_i} - e^{-\varphi_i}}{2j} \right) \\ &= \frac{G|Z_i|}{2} \sin\left(2\pi\frac{2f_i}{f_s}k + \varphi_i\right) + \underbrace{\frac{G \cdot |Z_i|}{2} \sin(\varphi_i)}_{\hat{Q}_i[k]} \end{aligned} \quad (10)$$

Naturally, Eqs. 9 and 10 contain additional product terms for interactions between all N_f frequency components, but these are omitted for clarity as they will be filtered out in the following step. The mixing process is exemplified in Fig. 5C for the in-phase impedance corresponding to f_4 : $I_4[k]$. The spectrum of the output of the mixer contains the baseband, time-independent term of Eqs. 9 and 10 and the high-frequency products. Let $\hat{I}_i[k]$ and $\hat{Q}_i[k]$ be the DC components extracted through an ideal low-pass filter. The real filter applied to the signals is discussed in section S1.5. A communications block outputs $\hat{I}_i[k]$ and $\hat{Q}_i[k]$ to the client software running on a PC. The result (Fig. 5D) may be converted to magnitude and phase quantities using Eq. 11 or to any passive one-port circuit model (e.g., RC parallel). In the following section, we explain our method to obtain localized strain from the n -frequency impedance signals \hat{I} and \hat{Q} .

$$\begin{aligned} |Z_i| &= \frac{2}{G} \sqrt{\hat{I}_i^2(k) + \hat{Q}_i^2(k)} \\ \varphi_i &= \tan^{-1} \left[\frac{\hat{Q}_i(k)}{\hat{I}_i(k)} \right] \end{aligned} \quad (11)$$

Localized strain reconstruction

Several methods have been used to reconstruct capacitance (and thus strain) from the electrical impedance data shown in Eq. 11. A graphical approach completed by solving a linear system of equations arising from the change of capacitance at the excitation frequencies is fast and efficient (17) but works best when the resistance of each segment remains constant. With most types of stretchable capacitive sensors, the compliant electrodes have strain-dependent piezoresistive behavior causing this assumption to be violated. Alternatively, optimization methods may solve for the unknown capacitances (and even resistances) of the model's system of nonlinear equations (35). In this case, the input resistance $\Re\{Z_1(\omega)\}$ and reactance $\Im\{Z_1(\omega)\}$ of the transmission line at each of N_f frequencies are measured, following Eq. 2. From these $2 \cdot N_f$ measurements, N_f

unknown resistances and N_f unknown capacitances are estimated. Conventional structured system identification algorithms such as subspace identification may be used to identify the capacitance values in real time (39). These methods require a nonconvex optimization problem to be solved at every time step, which may be impractical for high-speed online measurement. The optimization is not guaranteed to converge and often converges to a local optimum as the number of identified parameters increases (40). Other approaches have used machine learning methods such as support vector machines or artificial neural networks (20, 41). Such techniques are powerful but rely on the extensive collection of training data. Once trained, they are not easily modifiable to use with different sensors or number of segments.

We chose to use machine learning, specifically a multilayer perceptron (MLP) algorithm, to reconstruct strain at each sensor segment from the impedance signals. Despite the drawbacks mentioned above, MLP was selected because the sensors have nonlinear response and, thus, one model could both produce strain estimates and compensate for sensor nonidealities. Often strain is not the outcome of interest and is merely a proxy for another signal (e.g., joint angle), which is then predicted using a machine learning algorithm. The MLP may operate directly on the impedance signals to compute the final measurement without using strain or capacitance as an intermediate step. Neural network-based models have shown good results in previous work for refining strain sensor signals (42, 43). The MLP model avoids the need for online optimization, and once trained, inference can run very quickly. Our MLP architecture incorporates ℓ_1 and ℓ_2 norm-weighted regularization penalties. While tuned empirically, the former is intended to encourage sparsity in the output to reduce false positive strain signals when the segment is indeed at rest. The latter is applied as a general regularizer to reduce the degree of overfitting. Further details about the data collection protocol and model architecture are shown in Materials and Methods.

Having designed a system capable of high-speed impedance measurement to enable distributed sensing, we ran a bench experiment to validate the device, collect training data, and quantify strain reconstruction accuracy. We placed the four HACS fibers described previously in the test fixture and subjected them to various combinations of strains (see Materials and Methods and section S6 for test procedure and experimental setup details, respectively). We trained a simple MLP model (full details in Materials and Methods) to directly estimate the strain localized to each of the four segments from the in-phase and quadrature impedance components at each of the four excitation frequencies $\hat{T}_i[k], \hat{Q}_i[k]$ $i \in \{1, \dots, 4\}$ (totally, eight inputs and four outputs). We found a test set strain reconstruction root mean squared error (RMSE) of 1.04% with coefficient of determination (R^2) of 0.992. The test set actual and predicted strain patterns are shown in Fig. 6, and full results are listed in table S4. We noticed that the accuracy was generally higher on segments located more distal from the reader along the chain. This result may be explained by the technical specifics of the readout circuit. The lower-frequency excitation signal that preferentially measures the distal segment is more highly oversampled, increasing signal-to-noise ratio (see section S1 for details). We also compared the reconstruction accuracy between the cases with one and two segments that were simultaneously strained. In the training and validation sets, reconstruction RMSE was ~30% higher when straining two segments simultaneously, but this was not seen in the test set. This behavior

possibly indicates the model overfitting to single segment straining, which was more frequent in the dataset. From the correlation plots in Fig. 6B, it is evident that goodness of fit increases with strain in all four segments. This observation is partially attributable to variability in the segments' length at the rest position, such that they do not all begin at exactly 0% strain.

Joint angle monitoring

After observing promising results from the validation test under controlled conditions with four segments, we began a test of the previously introduced instrumented garment to reconstruct arm joint angles from the single sensing fiber. The participant performed three movements: shoulder adduction/abduction from approximately 0 to 90° with respect to the torso, elbow flexion throughout its entire range (approximately 180°), and wrist flexion from approximately 0 to 45° with respect to the forearm axis. These movements were chosen to capture the three major arm joints with a relatively large range of motion. Although the sensing fiber has been shown to have sufficient frequency response to detect strain rates above 5 Hz (32), we attempted to further limit the frequency of the movements to below 1 Hz to avoid rate-dependent effects. Reference joint angles were measured using a gold standard infrared camera optical motion capture (OMC) system. We trained a similar MLP model to that previously described, this time for joint angle prediction rather than strain (see Materials and Methods for details). We show in Fig. 7 the results from the last set of test data. We achieved joint angle regression RMSEs of 4.9, 6.5, and 6.1° for the shoulder, elbow, and wrist, respectively. As a percentage of the approximate ranges of motion, the normalized RMSE was 6.5%, 5.4%, and 8.1%. R^2 values were found to be 0.949, 0.966, and 0.831, with full cross-validation plots and results available in fig. S11 and table S5. In this work, limited data from one participant and simple data processing methods were used to show the concept of distributed sensing in a wearable application without placing too much focus on maximizing joint angle accuracies. Nevertheless, our single-fiber system approaches the RMSE values of around 2 to 5° reported for joint angle monitoring with multiple conventional, redundant sensors clustered around the joint (8, 9) (albeit under cases of well-controlled movements), yet without the associated wiring and connection hurdles. Note that the OMC markers were placed on top of the instrumented shirt. Although tight-fitting, we expect errors from the motion capture measurements because of marker displacements to be higher than standard biomechanics protocols with markers placed on the skin. The distributed sensing technology is naturally extensible to having more sensing regions per joint in a dense area without additional discrete sensors nor connections. We see that the reconstructed joint angles sometimes fail to track the peaks of the reference (see, e.g., the shoulder traces from fig. S11). When this occurs during extension peaks, it is probably that some of the sensors had insufficient prestrain to avoid becoming slack at full extension. The wrist not only had the poorest tracking accuracy but also was the most difficult to accurately record the OMC reference because the entire hand is resolved as a rigid body with only one marker. Our prototype garment is the first wearable device that uses distributed strain sensing to estimate multiple joint angles using a single-fiber sensor. We believe that with more extensive and accurate data collection, the technology has great promise to allow fibers in clothing to be used as sensors in a fully textile, unobtrusive package.

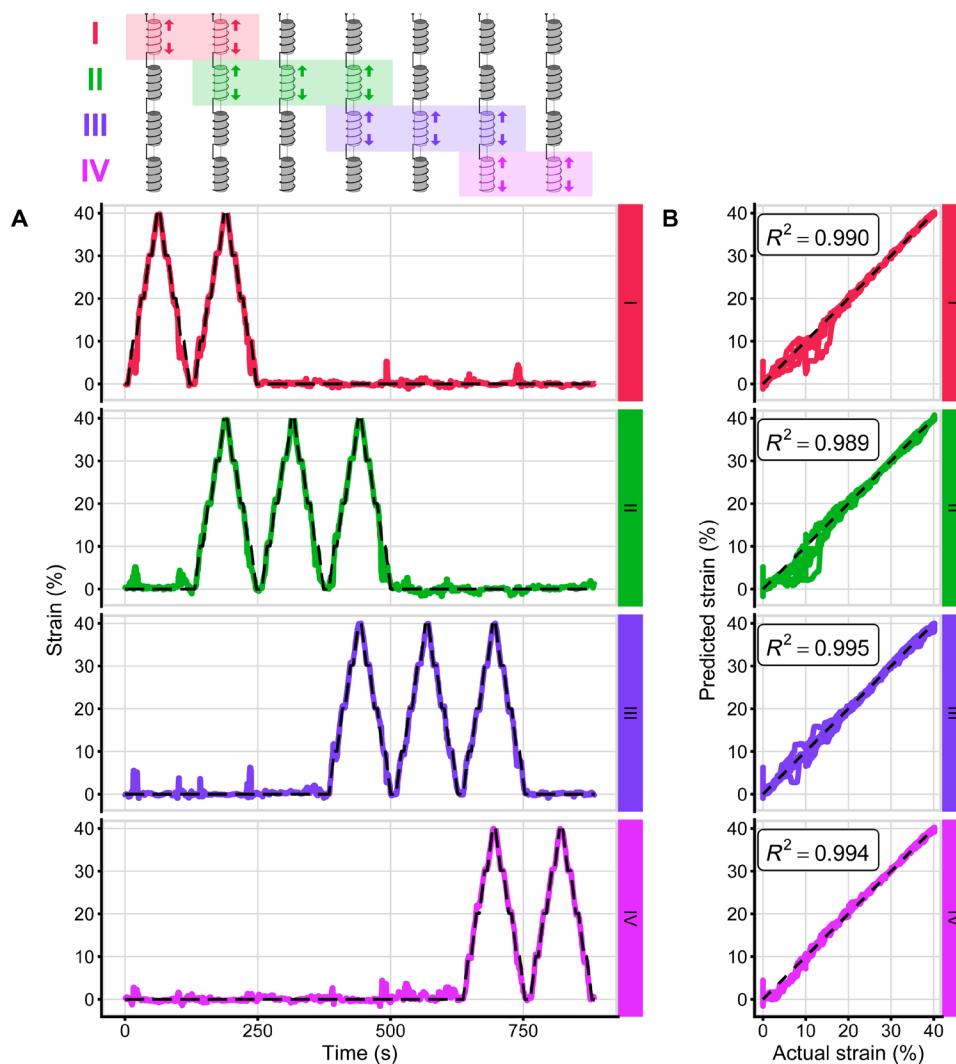


Fig. 6. Strain reconstruction tests. (A) Reconstructed (solid) and UTM reference (dashed black) strain for each sensor segment I to segment IV during the system validation experiment (test set shown). (B) Scatterplots of correlation between predicted and reference strain for each sensor and their associated R^2 values.

DISCUSSION

In this work, we reported a distributed sensing technology and demonstrated its use in a wearable application. We combined an electronic system with our capacitive fiber strain sensor to enable distributed sensing in textiles. We developed the first compact impedance analyzer circuit custom designed for distributed strain sensing in a wearable context. We applied the sensors in a way that allows sensitivity to be modulated across the fiber length to reject unwanted strain signals, such as those arising at undesired areas or from folds in the garment. The localized sensitivity of the desired sites allows a minimal number of frequencies and simpler electronics to reconstruct strain with around 1% error in controlled bench tests. Our device is validated with a UTM-controlled fixture to present quantitative strain reconstruction results, whereas previous distributed strain sensing reports have mostly shown qualitative tests. Applied in a prototype garment, our system estimates multiple joint angles with a single fiber, often to within five of an OMC system for major joint axes of interest.

As this is primarily a study to first demonstrate distributed sensing in a wearable device, there are certain limitations that may be addressed in future research. Scaling up the number of sensor segments is an obvious evolution of the technology. Although shown with one fiber and three joint measurements, the distributed sensing technique is naturally extensible to multiple fibers each having many measurement sites. This will be of focus for future research, exploring the limit of sensing region density. One can envision the future development of multisensing fabrics capable of measuring strain maps across the body in real time. There remain questions about the effect on strain reconstruction accuracy when multiple sensing regions are strained at once under nonideal conditions. We observed a moderate decrease in test set accuracy in the case of simultaneous strain, but we only explored the case of straining two adjacent segments. Evidence in other studies and our structural identifiability analysis supports the claim that the masking of one sensor segment by another appears not to be a major obstacle to the practical use of this distributed strain sensing system, but further investigation

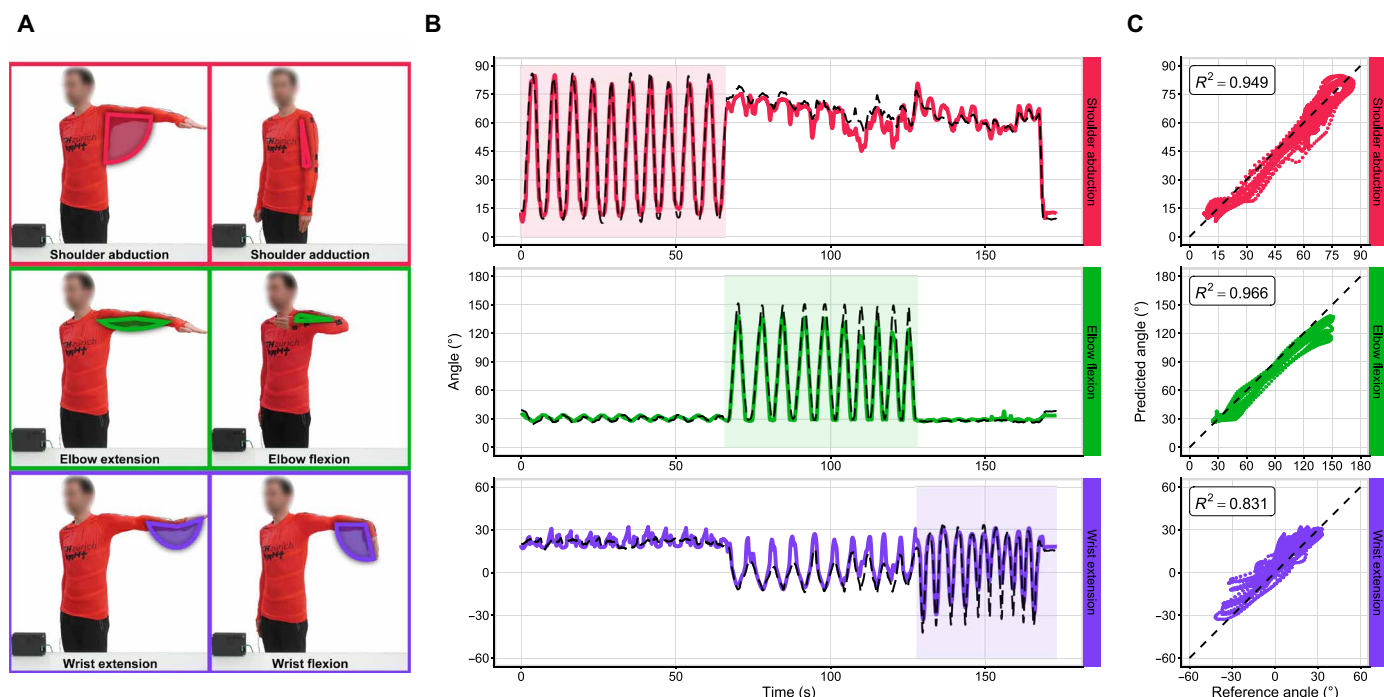


Fig. 7. Joint angle monitoring with the wearable prototype. (A) Visual demonstration of the three joint angles under consideration. (B) Predicted (solid) and OMC reference (dashed black) angles for each joint, from the final fold of testing, where shaded regions indicate the part of the test where that joint was voluntarily moved. (C) Scatter plots of predicted versus reference angles with associated R^2 values, where the black dashed line indicates perfect correlation.

would be of high interest. Although the MLP model we used to reconstruct strain and joint angles from impedance data is fast to run during inference, able to correct for nonlinear effects of the sensors, and able to compute the desired outcome measure directly, using supervised machine learning algorithms for this task introduces limitations. In our implementation, the algorithm must be retrained for use with different sensors types or number and positions of segments, as it has no innate knowledge of the dynamics. Training requires precollected data. Thus, one loses dynamic reconfigurability with this model, which is an important benefit of distributed sensing and of great interest for future work. Future research may target improved algorithms for capacitance reconstruction such that the size and number of segments can be dynamically changed. Last, we anticipate a further study including testing to evaluate the robustness of distributed sensing in more real-world scenarios, for example, with tracking of random or everyday arm movements.

While we aimed to keep the electronics simple by using a field-programmable gate array (FPGA) and minimal analog circuitry to allow translation to a fully on-chip solution more easily; it would be relatively straightforward to implement a wireless battery-powered system in the future. The electronics as designed could be made much smaller to become truly portable by integrating everything on a single printed circuit board (PCB), removing extraneous components, and changing the form factor so that it better fits a compact enclosure. Despite this, challenges exist with miniaturization of an accurate, wide-band impedance spectroscopy device. A main benefit to this conceptualization of distributed textile sensing is that the complex electronics may be decoupled from the all-textile garment, interfaced with only two connection points. The elimination of connection points within the garment and localization of all remaining

connections in a proximal hub markedly simplifies e-textile production, facilitating the progress of all-textile wearable sensor systems.

MATERIALS AND METHODS

Fiber sensor and prototype garment fabrication

The helical auxetic capacitive sensors were fabricated as described in (32). A stretchable conductive fiber (with a diameter of 0.75 mm), produced by applying a polypyrrole coating to an elastic fiber, was wound with a coil of 35 American wire gauge (AWG)-insulated copper wires. The core functions as one electrode of a capacitor with relatively high resistance and the coil functions as the other electrode with low resistance. The enamel insulation on the copper wire provides a dielectric layer. A thicker core was formed with three parallel coated elastic fibers for a final diameter of ~ 2 mm. For the bench tests, four separate core segments of relaxed length $\ell_0 = 10$ cm were wound with 4-mm pitch. For the prototype garment, a continuous core of 80 cm was wound with three sensitive regions of relaxed length $\ell_0 = 10$ -cm and 8-mm pitch. The sensing fiber was anchored with $\sim 10\%$ prestrain when the joint of interest was extended. Between the sensitive regions were two insensitive regions of varying lengths and a 3.5-mm pitch. The continuous sensor had an unstrained linear DC core resistance of $0.75 \text{ kilohm}\cdot\text{cm}^{-1}$ and a capacitance of $4.7 \text{ pF}\cdot\text{cm}^{-1}$. Capacitance and resistance versus strain of a sample sensor as measured with the LCR and our device are presented in fig. S6. For integration in the garment, we spaced the sensitive regions empirically so that they were centered around and fully overlapped the shoulder, elbow, and wrist joints. The sensing fiber was attached to the garment using clips sewn to elastane fabric backing patches. Photographs of the donned garment may be seen in fig. S10.

Electronics design and implementation

The digital signal processing (SWG, DAC, and PSD) was prototyped in Simulink (MathWorks, Natick, MA, USA) and implemented with custom Verilog code on FPGA fabric (Lattice iCE40HX-8 K, Lattice Semiconductor, Hillsboro, OR, USA). The analog circuitry (TCA and ADC) was prototyped in SPICE and was realized on a custom 75-mm × 45-mm PCB shown in Fig. 3C. Further details are provided in section S1. Verilog code, board layout files, client software, SPICE simulations, and mechanical part files used in this project are available in our repository: <https://gitlab.ethz.ch/BMHT/textile-wearables/textile-electronics/sensor-readout-board>.

Validation data collection protocol

A UTM (Instron E3000, Instron, Norwood, MA, USA) was interfaced with a custom-made fixture that allows straining of each sensing region independently (see fig. S9). Four fiber strain sensor segments I to IV were mounted on sliding rails with a center section that is connected to the UTM crosshead. The entire fixture top plate was then manually adjusted to bring each sensing region to approximately zero strain. One or two adjacent sensing regions were positioned in the center section of the fixture and thus subject to strain at a given time (allowing simultaneous combinations of segments I and II, II and III, as well as III and IV). The readout electronics are synchronized to the UTM with an electronic trigger signal, and the data are recorded by the client software running on a PC. The sensor was characterized electrically using an LCR meter as a reference (Hioki IM3536, Hioki, Ueda, Nagano, Japan). The UTM was programmed to follow an up-down staircase strain pattern, with steps of 10%, a ramp rate of $1\% \text{ s}^{-1}$, and a maximum strain of 40%. At each step, the strain was held for 5 s. Because of limitations of the fixture, we could only perform the simultaneous strain combinations I and II, II and III, as well as III and IV. The staircase pattern was repeated six times per sensing region combination. Data and scripts required to reproduce the figures in this manuscript are available in our repository: <https://gitlab.ethz.ch/BMHT/publications/distributed-sensing-along-fibres>.

Strain reconstruction model

A very simple MLP model was compiled using Keras/Tensorflow with architecture consisting of an eight-unit input layer, two hidden layers of sizes (16, 32) units and using tanh and rectified linear unit (ReLU) activation, respectively, and a four-unit output layer with linear activation. The second hidden layer had ℓ_2 regularization with weight 1×10^{-5} . The six trials collected as described in the above section were split into training (trials 1 to 4), validation (trial 5), and test (trial 6) sets. The model was trained with a batch size of 256 using the Adagrad optimizer with a learning rate of 0.1. Training was terminated when 50 epochs elapsed without an improvement in validation set mean squared error (MSE). The predicted strain model output was filtered with a moving median filter (window size of 2 s) before computing the metrics presented in table S4.

Wearable prototype data collection protocol

The subject donned the upper-body garment, and reflective OMC (Vicon Ltd., Oxford, UK) markers were placed according to the upper-body Plug-In Gait model. The subject performed 10 repetitions each of shoulder adduction, elbow flexion, and wrist flexion. These movements were repeated for 10 sets, with a brief rest period in between. The impedance signals from the readout board were synchronized electronically with the OMC system using its trigger

output. The joint angle reference signals were preprocessed with a Savitzky-Golay filter (window length of 2 s and fourth-order polynomial), and the impedance signals were Butterworth low pass-filtered (fourth-order, 2 Hz cutoff).

Joint angle reconstruction model

The MLP model used for strain reconstruction was slightly modified to be used in joint angle reconstruction. The output layer was adjusted to three units, corresponding to the three joint angles of interest. ℓ_1 and ℓ_2 regularization was applied to the second hidden layer with weights of 0.04 and 0.15, respectively, and both hidden layers used ReLU activations. The 10 trials of data collected as described in the above paragraph underwent a leave-one-out cross-validation scheme. At each cross-validation round, one trial was reserved for test data, and the remaining nine were split into test (80%) and validation (20%) sets. The input data were Z score-normalized (with scaling determined from training set only). In addition, the 10th epoch was reserved for testing; the results of this set are presented in the “Joint angle monitoring” section and Fig. 7, and no model tuning was performed using test data. The model was trained with a batch size of 64 using the Adam optimizer with a learning rate of 0.005. Training was terminated when a weighted average (shoulder, 1/3; elbow, 1/3; wrist, 2/3) of validation set MSE did not improve for 250 consecutive epochs.

Supplementary Materials

This PDF file includes:

Sections S1 to S9

Figs. S1 to S11

Tables S1 to S5

References

REFERENCES AND NOTES

1. D. Kim, J. Kwon, S. Han, Y. L. Park, S. Jo, Deep full-body motion network for a soft wearable motion sensing suit. *IEEE/ASME Trans. Mechatron.* **24**, 56–66 (2019).
2. Z. He, G. Zhou, J. H. Byun, S. K. Lee, M. K. Um, B. Park, T. Kim, S. B. Lee, T. W. Chou, Highly stretchable multi-walled carbon nanotube/thermoplastic polyurethane composite fibers for ultrasensitive, wearable strain sensors. *Nanoscale* **11**, 5884–5890 (2019).
3. F. Yin, X. Li, H. Peng, F. Li, K. Yang, W. Yuan, A highly sensitive, multifunctional, and wearable mechanical sensor based on RGO/synergetic fiber bundles for monitoring human actions and physiological signals. *Sens. Actuators B Chem.* **285**, 179–185 (2019).
4. R. Madhavan, Epidermis-like high performance wearable strain sensor for full-range monitoring of the human activities. *Macromol. Mater. Eng.* **307**, 2200034 (2022).
5. L. Zhu, Y. Wang, D. Mei, L. Zhang, C. Mu, S. Wang, S. Dai, Z. Chen, Large-area hand-covering elastomeric electronic skin sensor with distributed multifunctional sensing capability. *Adv. Intell. Syst.* **4**, 2100118 (2022).
6. A. Alian, G. Mylonas, J. Avery, Soft Continuum Actuator Tip Position and Contact Force Prediction, Using Electrical Impedance Tomography and Recurrent Neural Networks, *Proceedings of the IEEE-RAS International Conference on Soft Robotics (RoboSoft 2023)*, Singapore, 3–7 April 2023 (IEEE, 2023).
7. L. F. Boesel, D. P. Furundžić, N. Z. Furundžić, A. Gedanken, I. Grabchev, A. Haj Taieb, A. Ivanoksa-Dacic, S. Malionowski, D. Marković, G. Mohr, Y. Oguz Gouillart, P. M. Pinho, A. Sezai Sarac, D. Staneva, S. Tedesco, J. Vincente Ros, “Smart textiles for healthcare and medicine applications (WG1): State-of-the-art report, CONTEXT Project” (Tech. Rep., European Cooperation in Science and Technology, 2020).
8. M. I. M. Esfahani, M. A. Nussbaum, A “smart” undershirt for tracking upper body motions: Task classification and angle estimation. *IEEE Sensors* **18**, 7650–7658 (2018).
9. Y. Jin, C. M. Glover, H. Cho, O. A. Araromi, M. A. Graule, N. Li, R. J. Wood, C. J. Walsh, Soft sensing shirt for shoulder kinematics estimation. Paper presented at the IEEE International Conference on Robotics and Automation Paris, France, 31 May 2020 to 31 August 2020.
10. M. S. Kim, K. Kim, D. Kwon, S. Kim, J. Gu, Y. S. Oh, I. Park, Microdome-induced strain localization for biaxial strain decoupling toward stretchable and wearable human motion detection. *Langmuir* **36**, 8939–8946 (2020).

11. S. Niu, N. Matsuhisa, L. Beker, J. Li, S. Wang, J. Wang, Y. Jiang, X. Yan, Y. Yun, W. Burnett, A. S. Y. Poon, J. B. Tok, X. Chen, Z. Bao, A wireless body area sensor network based on stretchable passive tags. *Nat. Electron.* **2**, 361–368 (2019).
12. L. M. Castano, A. B. Flatau, Smart fabric sensors and e-textile technologies: A review. *Smart Mater. Struct.* **23**, 053001 (2014).
13. R. S. Saxena, N. K. Saini, R. K. Khan, Analysis of crosstalk in networked arrays of resistive sensors. *IEEE Sensors* **11**, 920–924 (2011).
14. M. Dulal, S. Afroj, J. Ahn, Y. Cho, C. Carr, I. D. Kim, N. Karim, Toward sustainable wearable electronic textiles. *ACS Nano* **16**, 19755–19788 (2022).
15. A. R. Köhler, L. M. Hilty, C. Bakker, Prospective impacts of electronic textiles on recycling and disposal. *J. Ind. Ecol.* **15**, 496–511 (2011).
16. M. Nilsson, Tactile sensors and other distributed sensors with minimal wiring complexity. *IEEE/ASME Trans. Mechatron.* **5**, 253–257 (2000).
17. A. Tairych, I. A. Anderson, *Electroactive Polymer Actuators and Devices (EAPAD)* (SPIE, 2017), vol. 10163.
18. H. Nesser, G. Lubineau, Achieving super sensitivity in capacitive strain sensing by electrode fragmentation. *ACS Appl. Mater. Interfaces* **13**, 36062–36070 (2021).
19. H. Nesser, G. Lubineau, Minimizing the wiring in distributed strain sensing using a capacitive sensor sheet with variable-resistance electrodes. *Sci. Rep.* **12**, 13950 (2022).
20. H. A. Sonar, M. C. Yuen, R. Kramer-Bottiglio, J. Paik, An any-resolution pressure localization scheme using a soft capacitive sensor skin. Paper presented at the 2018 IEEE International Conference on Soft Robotics (RoboSoft 2018) Livorno, Italy, 24 to 28 April 2018.
21. D. Xu, A. Tairych, I. A. Anderson, Stretch not flex: Programmable rubber keyboard. *Smart Mater. Struct.* **25**, 015012 (2016).
22. J. Lee, S. J. Ihle, G. S. Pellegrino, H. Kim, J. Yea, C.-Y. Jeon, H.-C. Son, C. Jin, D. Eberli, F. Schmid, B. L. Zambrano, A. F. Renz, C. Forró, H. Choi, K.-I. Jang, R. Küng, J. Vörös, Stretchable and suturable fibre sensors for wireless monitoring of connective tissue strain. *Nat. Electron.* **4**, 291–301 (2021).
23. L. Yu, Y. Feng, L. Yao, R. H. Soon, J. C. Yeo, C. T. Lim, Dual-core capacitive microfiber sensor for smart textile applications. *ACS Appl. Mater. Interfaces* **11**, 33347–33355 (2019).
24. C. B. Cooper, K. Arutselvan, Y. Liu, D. Armstrong, Y. Lin, M. R. Khan, J. Genzer, M. D. Dickey, Stretchable capacitive sensors of torsion, strain, and touch using double helix liquid metal fibers. *Adv. Funct. Mater.* **27**, 1605630 (2017).
25. Q. Zhang, Y. L. Wang, Y. Xia, P. F. Zhang, T. V. Kirk, X. D. Chen, A low-cost and highly integrated sensing insole for plantar pressure measurement. *Sens. Bio-Sens. Res.* **26**, 100298 (2019).
26. J. Kim, S. Kim, Y. L. Park, Single-input single-output multi-touch soft sensor systems using band-pass filters. *npj Flexible Electron.* **6**, 65 (2022).
27. D. Kim, Y. L. Park, Contact localization and force estimation of soft tactile sensors using artificial intelligence. Paper presented at the IEEE International Conference on Intelligent Robots and Systems, Madrid, Spain, 1 to 5 December 2018.
28. K. K. Kim, M. Kim, K. Pyun, J. Kim, J. Min, S. Koh, S. E. Root, J. Kim, B. N. T. Nguyen, Y. Nishio, S. Han, J. Choi, C. Y. Kim, J. B. Tok, S. Jo, S. H. Ko, Z. Bao, A substrate-less nanomesh receptor with meta-learning for rapid hand task recognition. *Nat. Electron.* **6**, 64 (2022).
29. M. Cao, J. Su, S. Fan, H. Qiu, D. Su, L. Li, Wearable piezoresistive pressure sensors based on 3D graphene. *Chem. Eng. J.* **406**, 126777 (2021).
30. X. Li, X. Li, T. Liu, Y. Lu, C. Shang, X. Ding, J. Zhang, Y. Feng, F. J. Xu, Wearable, washable, and highly sensitive piezoresistive pressure sensor based on a 3D sponge Network for real-time monitoring human body activities. *ACS Appl. Mater. Interfaces.* **13**, 46848 (2021).
31. Y. A. Lin, Y. Zhao, L. Wang, Y. Park, Y. J. Yeh, W. H. Chiang, K. J. Loh, Graphene K-Tape meshes for densely distributed human motion monitoring. *Adv. Mater. Technol.* **6** (2021).
32. T. J. Cuthbert, B. C. Hannigan, A. Shokurov, C. Menon, HACS: Helical auxetic yarn capacitive strain sensors with sensitivity beyond the theoretical limit. *Adv. Mater.* **35**, 2209321 (2023).
33. M. Amjadi, K. U. Kyung, I. Park, M. Sitti, Stretchable, skin-mountable, and wearable strain sensors and their potential applications: A review. *Adv. Funct. Mater.* **26**, 1678–1698 (2016).
34. A. Tairych, I. A. Anderson, *Proceedings of SPIE, Electroactive Polymer Actuators and Devices (EAPAD)* (no. 10594, SPIE, 2018).
35. A. Tairych, I. A. Anderson, A numerical method for measuring capacitive soft sensors through one channel. *Smart Mater. Struct.* **27**, 035016 (2018).
36. R. Bellman, K. J. Åström, On structural identifiability. *Math. Biosci.* **7**, 329–339 (1970).
37. M. N. Chatzis, E. N. Chatzi, A. W. Smyth, On the observability and identifiability of nonlinear structural and mechanical systems. *Struct. Control Health Monit.* **22**, 574–593 (2015).
38. C. Hwang, B. Nakano, T. Asahi, Transformation of state-space model to Cauer I and II CFE canonical forms. *Int. J. Syst. Sci.* **15**, 797–804 (1984).
39. G. Calzavara, L. Consolini, J. Kavaja, Structured identification for network reconstruction of RC-models. *Systems and Control Letters* **147**, 104849 (2021).
40. L. Ljung, On convexification of system identification criteria. *Autom. Remote Control* **80**, 1591–1606 (2019).
41. E. L. White, M. C. Yuen, R. K. Kramer, 2017 *IEEE Sensors* (IEEE, 2017).
42. A. Rezaei, T. J. Cuthbert, M. Gholami, C. Menon, Application-based production and testing of a core-sheath fiber strain sensor for wearable electronics: Feasibility study of using the sensors in measuring tri-axial trunk motion angles. *Sensors* **19**, 4288 (2019).
43. B. C. Hannigan, T. J. Cuthbert, W. Geng, C. Menon, Understanding the impact of machine learning models on the performance of different flexible strain sensor modalities. *Front. Mater.* **8**, 44 (2021).
44. A. Hamed, E. Tisserand, Y. Berville, V. Nancy, Fast FPGA implementation of an original impedance analyser. *Sens. Transducers* **10**, 191–205 (2011).
45. R. Kusche, A. Malhotra, M. Ryschka, G. Ardel, P. Klimach, S. Kaufmann, A FPGA-Based Broadband EIT system for complex bioimpedance measurements—Design and performance estimation. *Electron.* **4**, 507–525 (2015).
46. R. Schreier, G. C. Temes, *Understanding Delta-Sigma Data Converters* (Wiley, 1997), vol. 53.
47. L. Risbo, *Sigma Delta Modulators - Stability Analysis and Optimization*, (Doctor of Philosophy, Technical University of Denmark, 1994).
48. B. C. Hannigan, C. L. Petersen, A. M. Mallinson, G. A. Dumont, An optimization framework for the design of noise shaping loop filters with improved stability properties. *Circuits Syst. Signal Process.* **39**, 6276–6298 (2020).
49. A. Behrouzrad, P. Sugru, M. Todorovic, K. G. McCarthy, P. Galvin, 2021 *32nd Irish Signals and Systems Conference* (ISSC, 2021).
50. A. Klein, W. Schumacher, Algebraic operations on delta-sigma bit-streams. *Math. Comput. Appl.* **23**, 49 (2018).
51. D. G. Zrilic, *Functional Processing of Delta-Sigma Bit-Stream* (Springer, 2020).
52. J. Jeong, N. Collins, M. P. Flynn, A 260 MHz IF sampling bit-stream processing digital beamformer with an integrated array of continuous-time band-pass modulators. *IEEE J. Solid-State Circuits* **51**, 1168–1176 (2016).
53. E. Hogenauer, An economical class of digital filters for decimation and interpolation. *IEEE Trans. Signal Process.* **29**, 155–162 (1981).
54. K. Tindell, “Microcontroller interconnect network (MIN) protocol”; <https://github.com/min-protocol/min/wiki>.
55. C. Wolf, M. Lasser, “Project IceStorm”; <http://bygone.clairexen.net/icestorm/>.
56. K. J. Keesman, *System Identification - An Introduction* (Springer-Verlag, 2011).
57. H. Hong, A. Ovchinnikov, G. Pogudin, C. Yap, SIAN: Software for structural identifiability analysis of ODE models. *Bioinformatics* **35**, 2873–2874 (2019).
58. N. Martínez, A. F. Villaverde, Nonlinear observability algorithms with known and unknown inputs: Analysis and implementation. *Mathematics* **8**, 1 (2020).
59. E. August, Parameter identifiability and optimal experimental design. Paper presented at the 2009 International Conference on Computational Science and Engineering, Vancouver, Canada, 29 to 31 August 2009.
60. A. F. Villaverde, N. D. Evans, M. J. Chappell, J. R. Banga, Input-dependent structural identifiability of nonlinear systems. *IEEE Control Syst. Lett.* **3**, 272–277 (2019).
61. J. Karlsson, M. Anguelova, M. Jirstrand, An efficient method for structural identifiability analysis of large dynamic systems. *IFAC* **45**, 941–946 (2012).

Acknowledgments: We would like to acknowledge the help of M. Geissmann at the Swiss Centre for Movement Analysis (SCMA) whose expertise in recording and processing the OMC reference data presented in the “Joint angle monitoring” section was greatly appreciated.

Funding: We acknowledge that they received no funding in support for this research. **Author contributions:** B.C.H.: Conceptualization, methodology, software, validation, formal analysis, investigation, data curation, writing—original draft, writing—review and editing, and visualization. T.J.C.: Conceptualization, methodology, and writing—review and editing. C.A.: Methodology, formal analysis, software, data curation, and writing—review and editing. C.M.: Conceptualization, methodology, resources, writing—review and editing, supervision, project administration, and funding acquisition. **Competing interests:** T.J.C. and C.M. are coinventors on a patent that covers the helical auxetic capacitive sensor technology from (32). The technology from (32) was used as cited in this manuscript. The authors declare that they have no other competing interests. **Data and materials availability:** All data needed to evaluate the conclusions in the paper are present in the paper and/or the Supplementary Materials, as well as repositories listed in Materials and Methods. The version of the data and scripts required to reproduce the figures in this manuscript is also archived on the Zenodo repository with DOI: <https://doi.org/10.5281/zenodo.10645219>. The version of the software, firmware, and hardware designs for the readout system are also archived with DOI: <https://doi.org/10.5905/ethz-1007-706>. Materials used in this study were not subject to restrictive patents nor materials transfer agreements.

Submitted 17 August 2023

Accepted 13 February 2024

Published 20 March 2024

10.1126/sciadv.adj9708